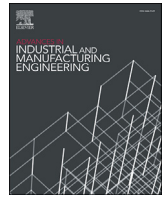


Contents lists available at [ScienceDirect](https://www.sciencedirect.com)

Advances in Industrial and Manufacturing Engineering

journal homepage: www.journals.elsevier.com/advances-in-industrial-and-manufacturing-engineering



Productivity enhancement of laser powder bed fusion using compensated shelled geometries and hot isostatic pressing



Anton Du Plessis^{a,*}, Bharat Yelamanchi^b, Christian Fischer^c, James Miller^c, Chad Beamer^d, Kirk Rogers^e, Pedro Cortes^b, Johan Els^f, Eric MacDonald^g

^a Research Group 3D Innovation, Stellenbosch University, 7602, South Africa

^b Youngstown State University, OH, 44555, USA

^c Scientific Forming Technologies Corporation, Columbus, OH, 43235, USA

^d Quintus Technologies, LLC, Lewis Center, OH, 43035, USA

^e The Barnes Global Advisors LLC, Sewickley, PA, 15143, USA

^f Centre for Rapid Prototyping and Manufacturing (CRPM), Central University of Technology, Bloemfontein, South Africa

^g W. M. Keck Center for 3D Innovation, University of Texas at El Paso, USA

ARTICLE INFO

Keywords:

Productivity enhancement
Laser powder bed fusion
Ti6Al4V
Hot isostatic pressing
Shelled powder metallurgy
Additive manufacturing

ABSTRACT

In laser powder bed fusion (L-PBF), the mechanical performance and especially fatigue properties of fabricated parts are significantly improved by hot isostatic pressing (HIP) as the density increases (pores are closed) and the microstructure improves. HIP ensures consistent and defect-free material, and consequently, this high temperature and high pressure process is often a requirement for safety-critical aerospace applications. The use of HIP to directly consolidate intentionally-unmelted interior powder in a L-PBF part was recently demonstrated. By confining the laser melting to only the outer shell (contour) of the structure, L-PBF production times can be dramatically reduced. A subsequent HIP cycle, which may be mandatory for reliability reasons, and therefore does not add additional costs, is then used to densify the entire structure. Production rates and energy efficiencies can therefore be improved in this way. This study explores the effect of relying on the HIP process to consolidate interior sections of test coupons, for which micro computed tomography (microCT), process simulation and tensile tests were conducted. MicroCT of coupons with varying shell thicknesses identify the minimum shell thickness required; and provide indications of the shrinkage ratio as a function of powder content relative to shell thickness. Preliminary results are included in which the shrinkage can be compensated for during design, by way of a “bloated cube” which collapses to a nominal cube geometry after HIP. The mechanical evaluation of the consolidated shelled parts indicates that their tensile performance is equivalent to those observed on fully dense printed parts. Up to an order of magnitude faster build rates are possible and any resulting shrinkage or distortion can be offset at design.

1. Introduction

Laser powder bed fusion (L-PBF) is a widely adopted form of additive manufacturing for the production of end-use, complex geometries in high performance metal alloys (DebRoy et al., 2017; Gu et al., 2012). Low-volume, high-value and complex products are paramount for advancing the aerospace industry with regards to fuel efficiency through techniques such as light-weighting, latticing and topology optimization (Du Plessis et al., 2018a; Flores et al., 2020; Plocher and Panesar, 2020; Van Grunsven et al., 2014). L-PBF is particularly well suited for intricately-detailed medium-sized structures fabricated in the most

advanced engineering alloys among all of the available additive manufacturing technologies (Standard A. ISO/ASTM 52900: 2015, 2012). One remaining challenge relative to other processes, but in particular when compared to traditional manufacturing, is the limited production rate which is restrained largely by limits to the laser scan speed and laser power (de Formanoir et al., 2020; Ma et al., 2015).

The productivity of L-PBF is directly impacted by the associated process parameters (e.g. hatch spacing, scan speed and layer thickness), which if optimized for improving production include balancing a tradeoff with the mechanical and dimensional performance. A diversity of strategies to improve the productivity of L-PBF have been explored including

* Corresponding author.

E-mail address: anton2@sun.ac.za (A. Du Plessis).

<https://doi.org/10.1016/j.aime.2021.100031>

Received 16 November 2020; Received in revised form 24 December 2020; Accepted 15 January 2021

2666-9129/© 2021 The Author(s). Published by Elsevier B.V. This is an open access article under the CC BY license (<http://creativecommons.org/licenses/by/4.0/>).

Table 1
Overview of all manufactured samples.

Specimens	Build Number	Shell thickness mm (quantity)					
		0.5	1	1.5	2	2.5	Full
10 mm cubes (shelled)	1	3	3	3	3	3	0
10 mm cubes (full density)	2	0	0	0	0	0	15
Machined tensile bars (60 × 10 mm cylinders - shelled)	1	0	0	3	0	0	0
Machined tensile bars (60 × 10 mm cylinders)	2	0	0	0	0	0	3
Not-machined tensile bars (60 mm dog bone - shelled)	1	0	0	3	0	0	0
Not-machined tensile bars (60 mm dog bone)	2	0	0	0	0	0	3
Complex bracket (shelled)	1	0	0	1	0	0	0
Complex bracket (full density)	2	0	0	0	0	0	1

larger build volumes (Poprawe et al., 2015), multiple lasers (Carter et al., 2020a) and spinning cylindrical powder beds (Carter et al., 2020b); however, although these clever techniques will eventually improve the economics of scale of laser powder bed fusion, each increases manufacturing cost and complexity. A recent study by de Formanoir et al. (de Formanoir et al., 2020) showed an interesting approach: a shelled region and interior regions of the same part were processed with different layer thickness, improving production rates with larger layer thickness in the interior, but increasing the formation of pores in this region, relating to the higher build rate.

Another approach to improving productivity was investigated by simply increasing the laser scan speed despite increasing the porosity in the process, and then subsequently eliminating the porosity with hot isostatic pressing (HIP) (Herzog et al., 2020). Hot isostatic pressing is a commonly required post-processing step and may therefore be required with or without faster processing, consequently not incurring additional cost. Hot isostatic pressing is a post-processing method which improves

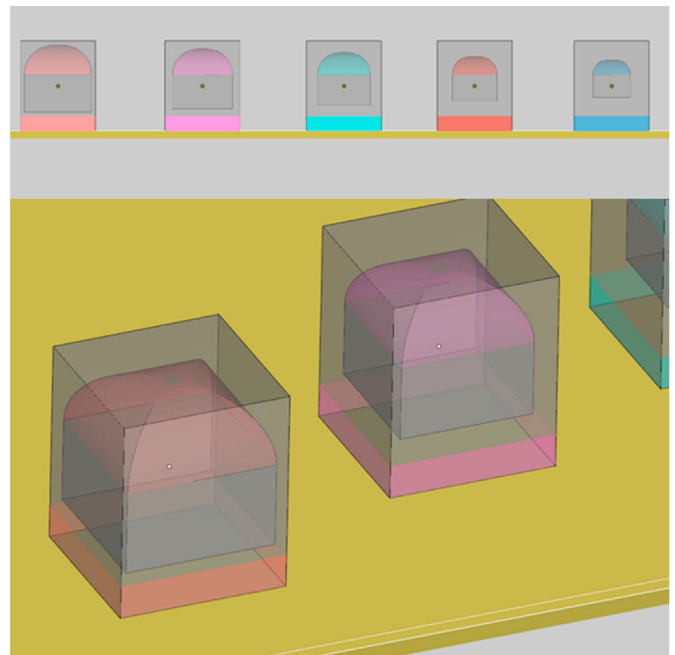


Fig. 2. Shelled cubes shown with interior cavity geometry - including 4 mm radius of curvature fillets near to improve build quality of top shelled surface. Shell thickness from left to right 0.5 mm, 1.0 mm, 1.5 mm, 2.0 mm and 2.5 mm, additional 2 mm at bottom for cutting from baseplate.

the quality of metal and ceramic structures and is well suited for additively manufactured structures by conveniently accommodating complex geometries for EB-PBF (Ahlfors et al., 2019; Leicht et al., 2016; Goel et al., 2019; Seifi et al., 2017a; Persenot et al., 2018; Hosseini et al., 2012; Eklund et al., 2018; Mireles et al., 2015; Medina, 2013) and L-PBF

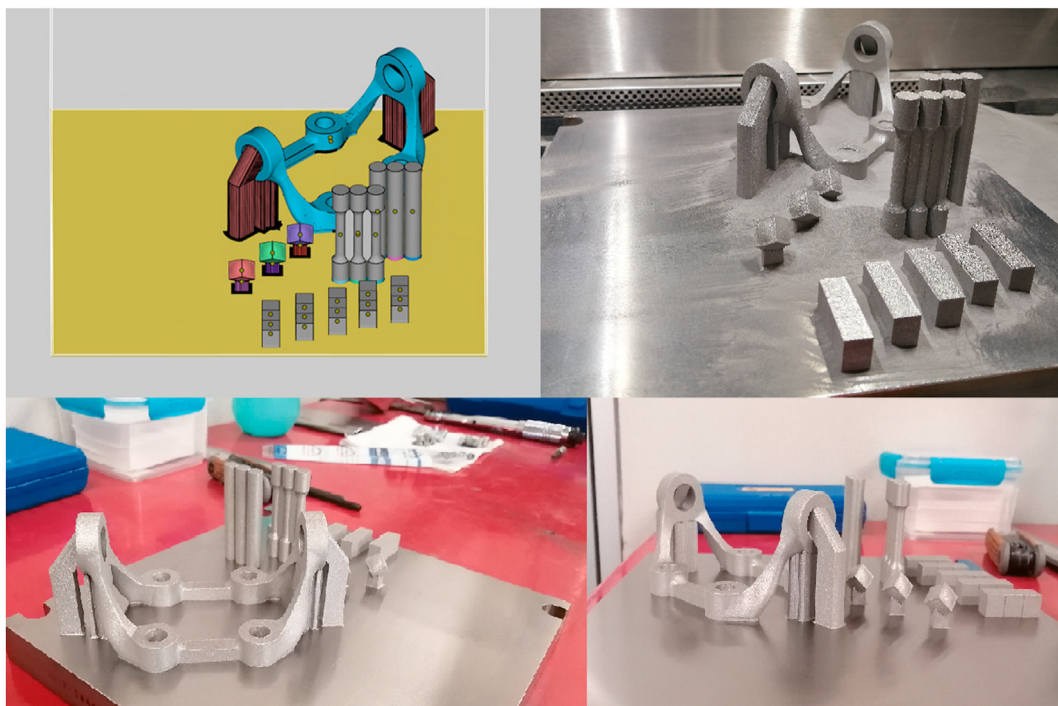


Fig. 1. Shelled build showing all shelled parts on build plate, and identical solid build was also manufactured.

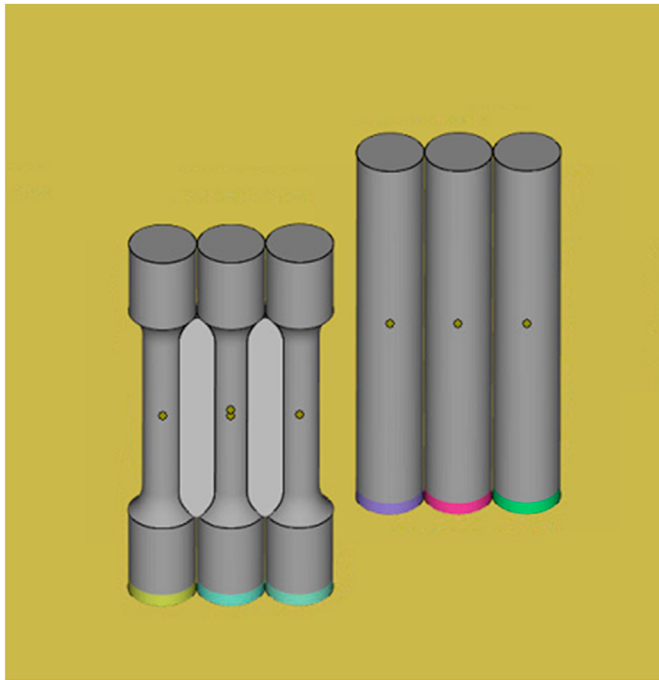


Fig. 3. Tensile samples in dogbone geometry (no machining) and in cylinder geometry (for machining of dogbone geometry).

(Kaplanski et al., 2018; Kunz et al., 2016; Zhou et al., 2018; Yan et al., 2019; Uzan et al., 2018; Chastand et al., 2018; Montero-Sistiaga et al., 2019; Mostafa et al., 2017; Schneller et al., 2019) for a diversity of metal alloys. Simultaneously, high temperature and high gas pressure are applied to the structure ensuring densification and microstructural homogenization. The process has a long legacy in traditional manufacturing for powder metallurgy and cast metals to improve density and microstructure homogenization (Atkinson and Davies, 2000). HIP has been demonstrated to eliminate pores as large as five mm in diameter in Ti6Al4V parts created with both traditional and additive manufacturing (du Plessis and Rossouw, 2015; Cai et al., 2016a; Cai et al., 2016b; Cai et al., 2018). The increased density from HIP is understood to improve fatigue performance (Masuo et al., 2018), and consequently, HIP is now widely accepted as a necessary post process in the aerospace additive manufacturing production chain (Ahlfors et al., 2019; Seifi et al., 2017b), a required step which could potentially be leveraged to realize additional benefits. The first demonstration of this concept was performed in early work with Ti6Al4V employing an ~2.5 mm shell and essentially demonstrating the concept of excellent densification in an efficient hybrid process combining L-PBF and HIP (Das et al., 1999). Others have used similar concepts to produce shelled near net shape “cans” by L-PBF, filled these with powders, closed and subjected them to HIP for densification, focusing on creating unique alloys and composites (Kunz et al., 2016, 2020), (Riehm et al., 2019).

X-ray tomography is a useful method for non-destructive evaluation of complex structures and when leveraged for powder bed fusion before and after HIP processing, the extent of porosity reduction can be

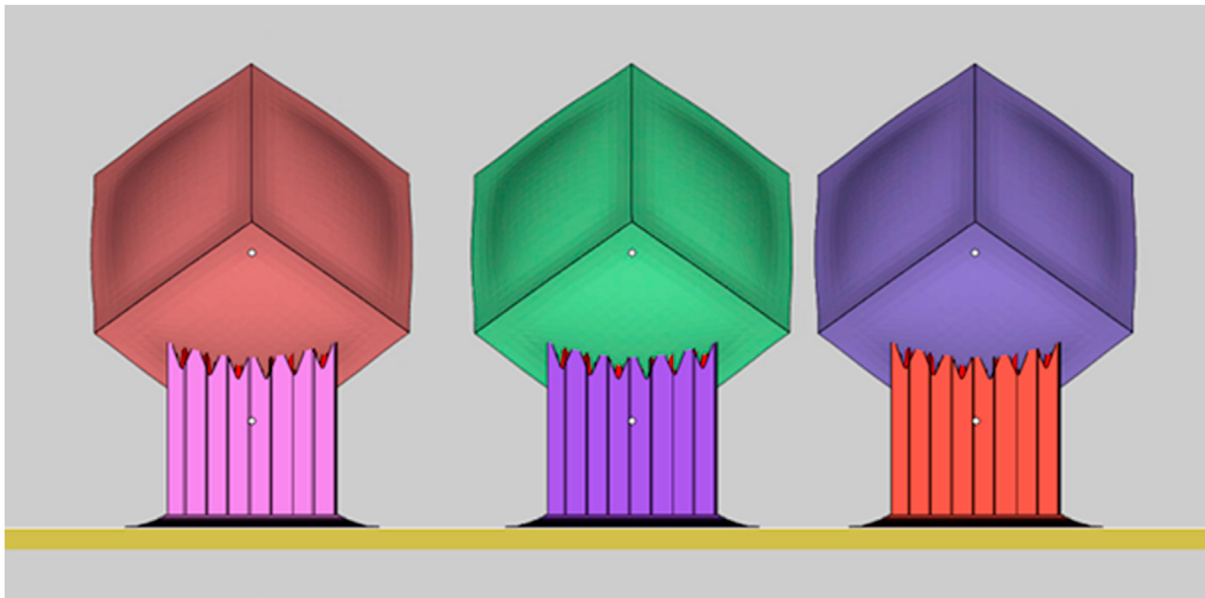


Fig. 4. Bloated cube - pre-compensated cube geometry manufactured using supports and angled to improve manufacturability and prevent overhangs.

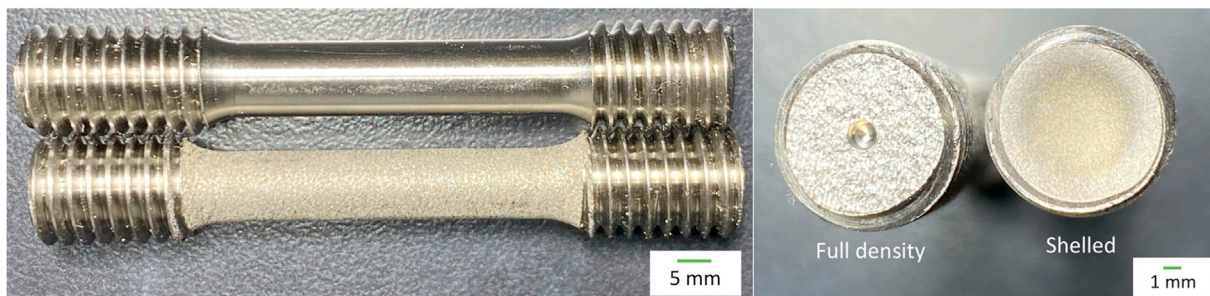


Fig. 5. Tensile bars investigated in this research program. Left: Machined (top). Not-machined (bottom). The samples were 60 mm in length and had 6 mm in gauge diameter. Right: Top view of the Full density and Shelled samples.

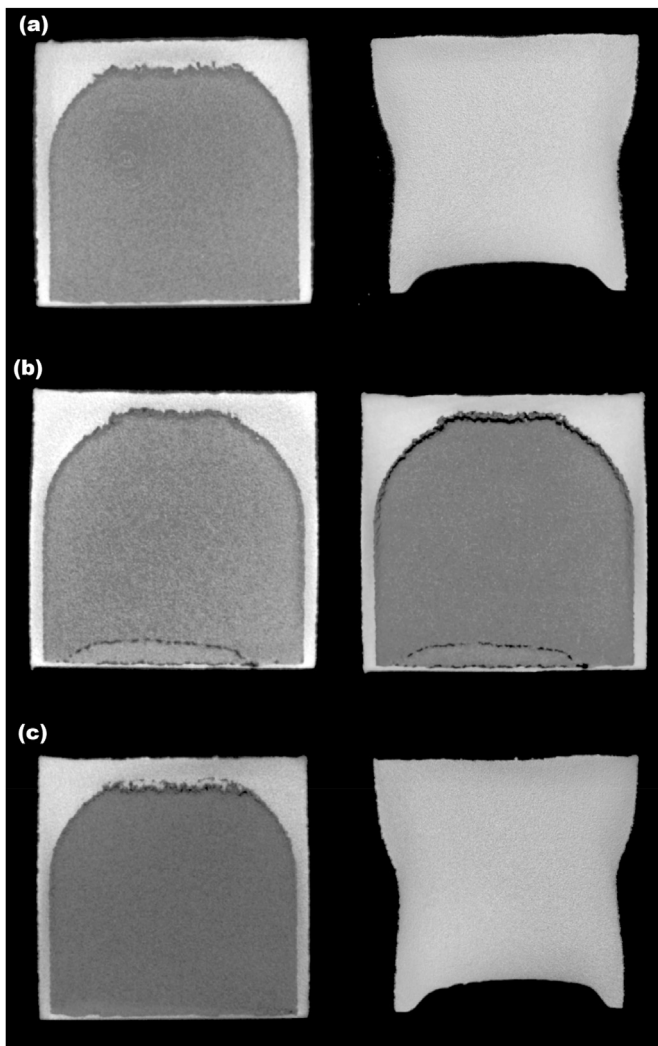


Fig. 6. Three cubes manufactured with 0.5 mm shell - shown before and after HIP. (a) Successful densification, (b) no densification due to bottom surface closure, (c) successful densification as indicated by homogenous material and lack of detected pores (5 μm voxel size).

quantified. For example, Seifi et al. (Mireles et al., 2015) found small porosity randomly within electron beam melting samples of Ti48Al2Cr2Nb which were imaged by tomography. Porosity as small as 20 μm in diameter was eliminated beyond the resolution of the scan. In the study of Ti6Al4V parts produced by L-PBF in (Medina, 2013), closed pores were identified while others remained unchanged and it was speculated that the unchanged pores were connected to the surface. Using samples with varying distributions of porosity, the effectiveness of closure was shown in (Kaplanski et al., 2018) demonstrating how surface-connected pore networks remain unchanged while other pores in the interior were entirely closed below the instrument resolution (24 μm).

In the work of du Plessis & MacDonald (du Plessis and Macdonald, 2020), the HIP-densification of different forms of typical L-PBF porosity was studied using X-ray tomography of 5 mm cubes (125 mm³ volume) before and after HIP. Excellent densification was demonstrated including the unexpected full densification with minimum shrinkage of a 2 mm powder-filled spherical cavity (assumed at ~50% density for powder and with a volume of 4.19 mm³). Following this interesting preliminary result, the current work extends this concept to use L-PBF to produce shelled parts filled with powder and relying on HIP to fully densify the

parts, saving significant production time on the L-PBF system and compensating for the shrinkage based on HIP simulations. Similar recent work with preliminary results can be found in conference presentations (Magnus Ahlfors Chad Beamer, 2020), however, the work was not presented at Rapid 2020 due to the pandemic and the cancellation of the conference. The unrepresented work did not include compensation for shrinkage and deformation, but this additional step would have been an obvious extension to the work.

Developing an understanding of the impact of relying on HIP to consolidate interior unmelted powder is the focus of this paper with the objective of improving production rates for this new hybrid process, while maintaining acceptable mechanical performance and dimensional compliance. The concept is demonstrated for a variety of geometries, using X-ray tomography before and after HIP. The geometries included 10 mm cubes with different shell thicknesses, tensile dogbone samples, cylinders from which dogbone samples were machined, a topology optimized bracket and pre-compensated cube geometries. These were manufactured in solid and shelled versions for comparison. Pre-compensated cube geometries were obtained using HIP deformation simulation: a shelled cube was modified to compensate for the shrinkage caused by the collapsing internal powder, which is loaded by default in the L-PBF system at an expected packing density of ~60%. The cube faces were bloated to arrive approximately to the intended geometry. In addition to X-ray CT, tensile testing and fracture surface analysis are reported. This experimental campaign using a variety of geometries is described in detail in this paper and the potential for improved productivity for L-PBF using this methodology is thereby proven.

2. Materials and methods

A variety of geometries were designed with and without shells, fabricated, hot isostatic pressed and evaluated both mechanically and with X-ray tomography. Design changes were included for some cubes ("bloated") to highlight the ability to compensate dimensionally for the internal shrinkage.

2.1. Fabricated geometries

Samples were manufactured in Ti6Al4V (ELI) on an EOS M290 system, with prescribed process parameters: laser power 280 W, scan speed 1.2 m/s, 0.03 mm layer height, hatch spacing 0.14 mm with 67° rotation of hatch direction on each layer. Powder was the recommended gas atomized Ti6Al4V (ELI) with D90 value of 50 μm . Standard stress relief heat treatment was employed followed by wire cutting from baseplate. Shells for parts were generated using Materialize Magics software. Two builds were done - one with all samples shelled and one with all samples solid. There were four steps in the study, with samples associated with each step as summarized below (but all samples manufactured in two batches, see Table 1 and Fig. 1):

1. To understand the effect of varying shell thickness on the densification and shrinkage for cubes of 10 mm: 10 samples were produced with wall thickness by design selected as 0.50; 1.00; 1.50; 2.00; and 2.50 mm. This means the thickest shell sample has an internal cube of powder of 5 mm and the thinnest shell has a cube of powder of 9.5 mm wide. Fillets with radius of curvature of 4 mm were added to the inner top shell to ensure the structure is self-supporting and prevent build failure with a large horizontal region without any supports (Fig. 2).
2. Tensile samples were produced directly in dogbone geometry and by manufacturing cylinders for machining, both in vertical orientation. Cylinders of 60 × 10 mm were manufactured, and (after HIP) were machined into subsized ASTM E8 tensile dogbone geometry (gauge length four times diameter, with gauge diameter = 6 mm). Tensile dogbones were also manufactured directly in their final geometry and were not machined, to include the rough surface condition. Each

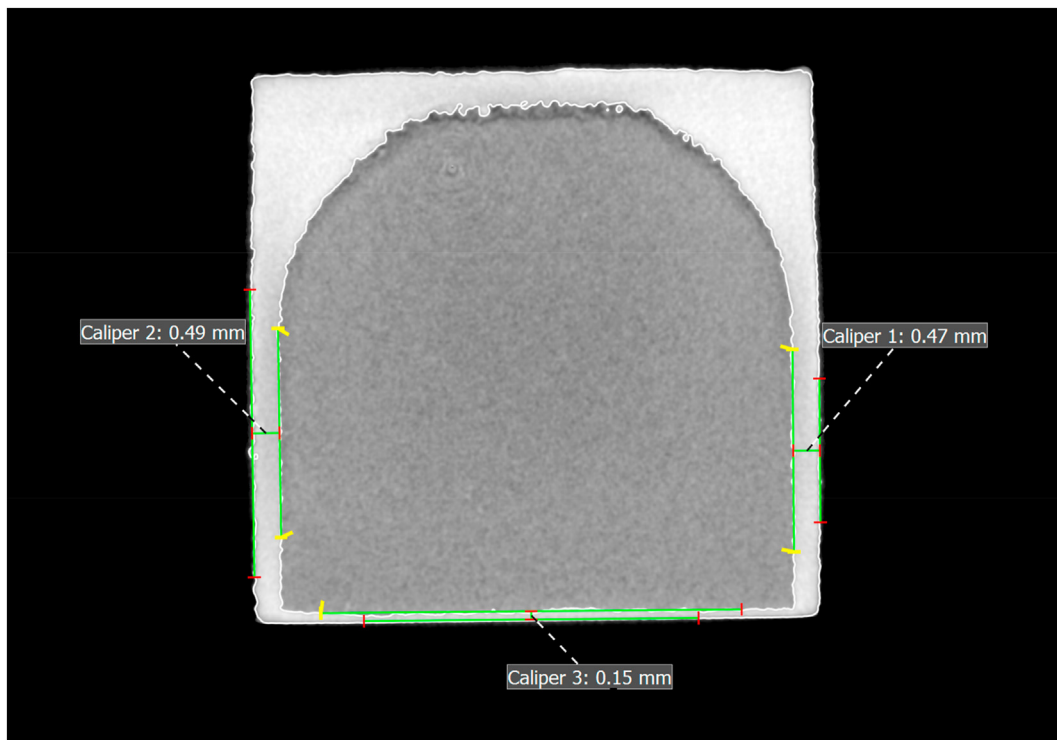


Fig. 7. Measurements of shell thickness with intended design thickness of 0.5 mm - bottom surface is 0.15 mm indicating cut from baseplate removed too much material.

build contained 3 blocks and 3 tensile samples, and the two builds were “solid” vs “shelled”, shell thickness selected at 1.5 mm (Fig. 3 and 5)

3. A pre-compensated cube geometry was obtained from simulation, resulting in a “bloated cube” - this sample was shelled with 1.5 mm and no internal fillets included, and hence to improve manufacturing and prevent build failure, the bloated cubes were built at an angle and with supports (Fig. 4). The supports were left in place to prevent possible damage which could affect the HIP process.
4. A complex shaped bracket used in a previous study (du Plessis and le Roux, 2018; du Plessis et al., 2019) was used in larger format, in two builds solid vs shelled - shell thickness 1.5 mm

2.2. Hot isostatic pressing

Hot isostatic pressing was performed at Quintis Technologies (Ohio USA), using the routine parameter set for Ti6Al4V: using high purity Argon gas with pressure of 100 MPa, ramped up to 920 degrees C over 2 h then soaked for 2 h, followed by cool-down to room temperature for 30 min.

2.3. X-ray tomography

X-ray tomography was performed at the Stellenbosch CT facility (du Plessis et al., 2016), using a GE Nanotom S System with voltage and current set to 140 kV and 130 μ A, using a 0.5 mm copper beam filter and achieving 5.0 μ m voxel size. The use of X-ray tomography in additive manufacturing has been described in detail in (Du Plessis et al., 2018b). X-ray tomography was performed on samples both before and after HIP. Image analysis was performed in Volume Graphics VGSTUDIO MAX 3.3, in this case before-after scan data was aligned to allow direct comparison of scans.

2.4. Mechanical testing

Tensile testing was performed on an Instron machine 5500 R using cylindrical specimens following the ASTM E8/E8M (see Fig. 1). The testing was carried out with an extensometer attached to the samples.

2.5. Build time

In this work the actual build times were recorded for the solid and shelled builds and estimated times from the EOS software are also provided. Additionally, estimated times were calculated for hypothetical cubes manufactured up to the maximum size of the EOS M290 system: 240 \times 240 \times 290 mm solid and shelled (1.5 mm shell thickness). This was done as an extreme example showing the maximum potential time saving by using this method.

2.6. Finite-element modeling

Non-linear, finite element, thermo-mechanical analysis has long been established as a suitable method for predicting the deformation and densification behavior of porous metals (Leuders et al., 2013; Oh et al., 1987; 51.). The DEFORM® system (Version 12.0.1 and Sc, 2020) was used to simulate distortion of the HIP test samples from this study. Cubic geometries were modeled with a structured brick mesh, while the more complex bracket geometry was modeled with an unstructured tetrahedral mesh. DEFORM utilizes an advanced mixed-formulation tetrahedral element (Wu et al., 2000), which avoids the locking phenomenon associated with more basic tetrahedral element formulations.

The finite element model was created by Scientific Forming Technologies Corp. in DEFORM-3D V12.0.1. Flow stress data for Ti6Al4V was obtained from the DEFORM material library. The initial relative density (powder density/fully-consolidated density) was assigned by regions.

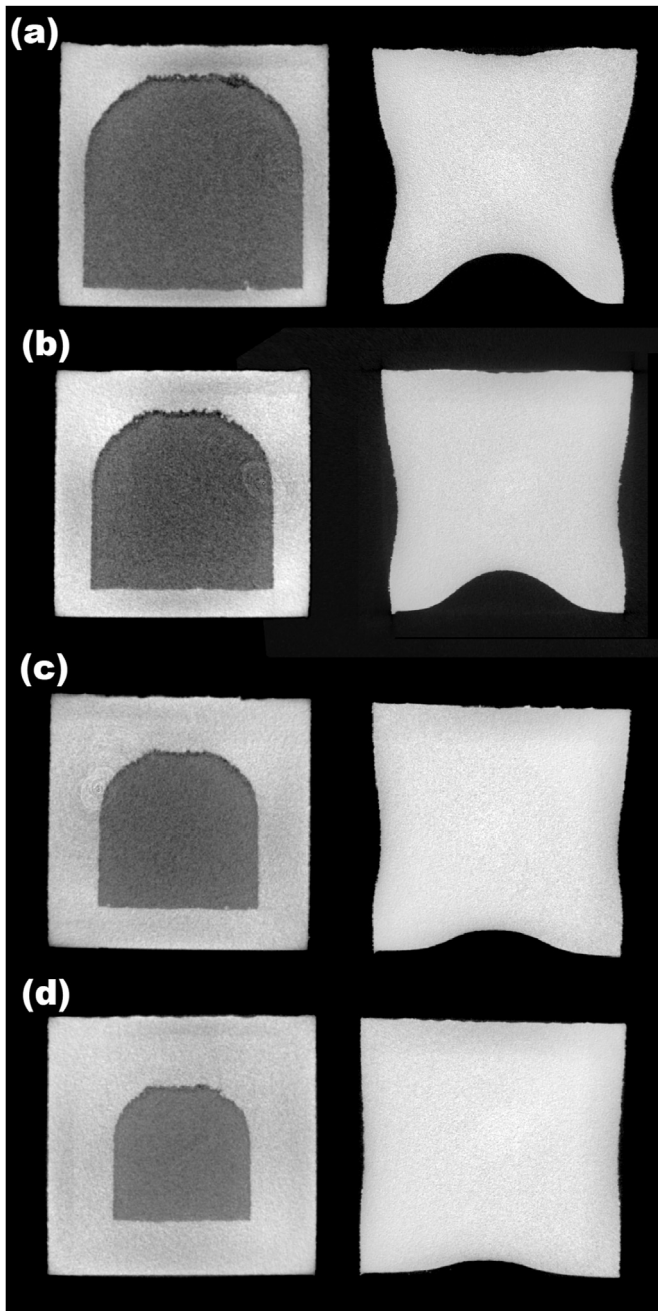


Fig. 8. Shelled cubes before (left) and after HIP (right), with intended shell thickness of (a) 1 mm, (b) 1.5 mm, (c) 2.0 mm and (d) 2.5 mm. One example of each is shown, all three of each type fully densified (12 samples).

Elements in the outer shell had a relative density of 1, while elements in the powder core had a relative density of 0.58 (Zhou et al., 2009). Local velocity boundary conditions constrained the part in three degrees of translation and three degrees of rotation without restricting overall part distortion. The workpiece and environment temperatures were 920 °C and pressure was ramped to 100 MPa over 60 s. Consolidation was assumed to have reached equilibrium when nodal velocities reached zero (Fig. 5).

3. Results and Discussion

3.1. Impact of shell thickness of 10 mm cube shrinkage

X-ray tomography was performed on all cubes before and after HIP, with selected images shown below to highlight the important results (Fig. 6–8). X-ray tomography shows that the HIP process fully densifies the material - no pores are detected at the voxel size of 0.005 mm. In Fig. 6 is shown the three cubes with intended shell thickness of 0.5 mm. Of the three samples, two successfully densified with corresponding deformation as seen in Fig. 6(a) and (c). In Fig. 6(b) an unsuccessful densification by HIP is shown - due to a hole in the bottom shell as seen in the image. Gas enters this hole and renders the HIP process ineffective on this sample. It should be noted that the shell thickness in the bottom surface here is only 0.15 mm as measured and shown in Fig. 7. This is not due to L-PBF inaccuracy but rather the cutting from the baseplate which removed too much material. This is an important lesson for future work using this approach - to ensure the bottom surface near the baseplate removal is given a thicker shell to compensate for this potential problem.

All other cubes with intended shells of 1.0 mm and above successfully densified, one example of each shell thickness is shown in Fig. 8. The maximum deformation becomes less as the shell thickness increases and hence the powder cavity size reduces. The largest deformation is found in the bottom surface, as the top surface includes fillets. The introduction of the fillets improved the deformation considerably - which is another important lesson from this work. Optimization of the fillet usage may reduce the deformation, but at the compromise of increasing manufacturing time as well.

3.2. Tensile samples and mechanical tests

Tensile samples and cylinders were manufactured and all shells checked in CT scans - all were well manufactured using 1.5 mm shell thickness, with one example of each shown in Fig. 9. Subsequent HIP was applied to all samples, which was followed by the cylinders being machined to dogbone geometry and mechanical tests as described below.

Fig. 10 shows the average mechanical properties of the tested materials, where it is observed that although the tensile strength of the machined specimens is slightly higher than that recorded on the directly manufactured dogbone geometry specimens, no apparent difference is observed in the strength between the full dense and the shelled parts. A similar mechanical profile was displayed by the yield strength. Fig. 10 also shows the elastic modulus and strain at failure of the tested specimens. The figure shows that a similar Young's modulus was recorded across the different investigated specimens. In contrast, the average failure strain of the shelled dogbone parts was lower than the reported by the rest of the specimens, a mechanical property probably associated with the α lath thickness determined by the equiaxed $\alpha+\beta$ phase which is usually the major factor determining the mechanical properties (Galarraga et al., 2017). These results suggest that the observed mechanical properties are within the range of previous studies (Liu and Shin, 2019; Leuders et al., 2013; Oh et al., 1987; 51.) and well within acceptable ranges. Fig. 11 shows also the stress-strain curves for the parts.

A microscopic analysis was performed on the fracture surfaces (see Fig. 12), and it was observed that no difference in failure mode was shown on the samples manufactured under different conditions. All samples show a marked degree of ductile fracture. An additional SEM microscopy was performed on the shelled and full-dense parts (Fig. 13), and it seemed that the HIPed samples appear to display a slightly larger degree of porosity. However, such defects did not seem to have a distinct impact on the mechanical performance of the samples, based on the tensile strength shown in Fig. 10.



Fig. 9. Cylinders and tensile dogbones manufactured with 1.5 mm shell, microCT scan shows good shell and geometry filled with powder.

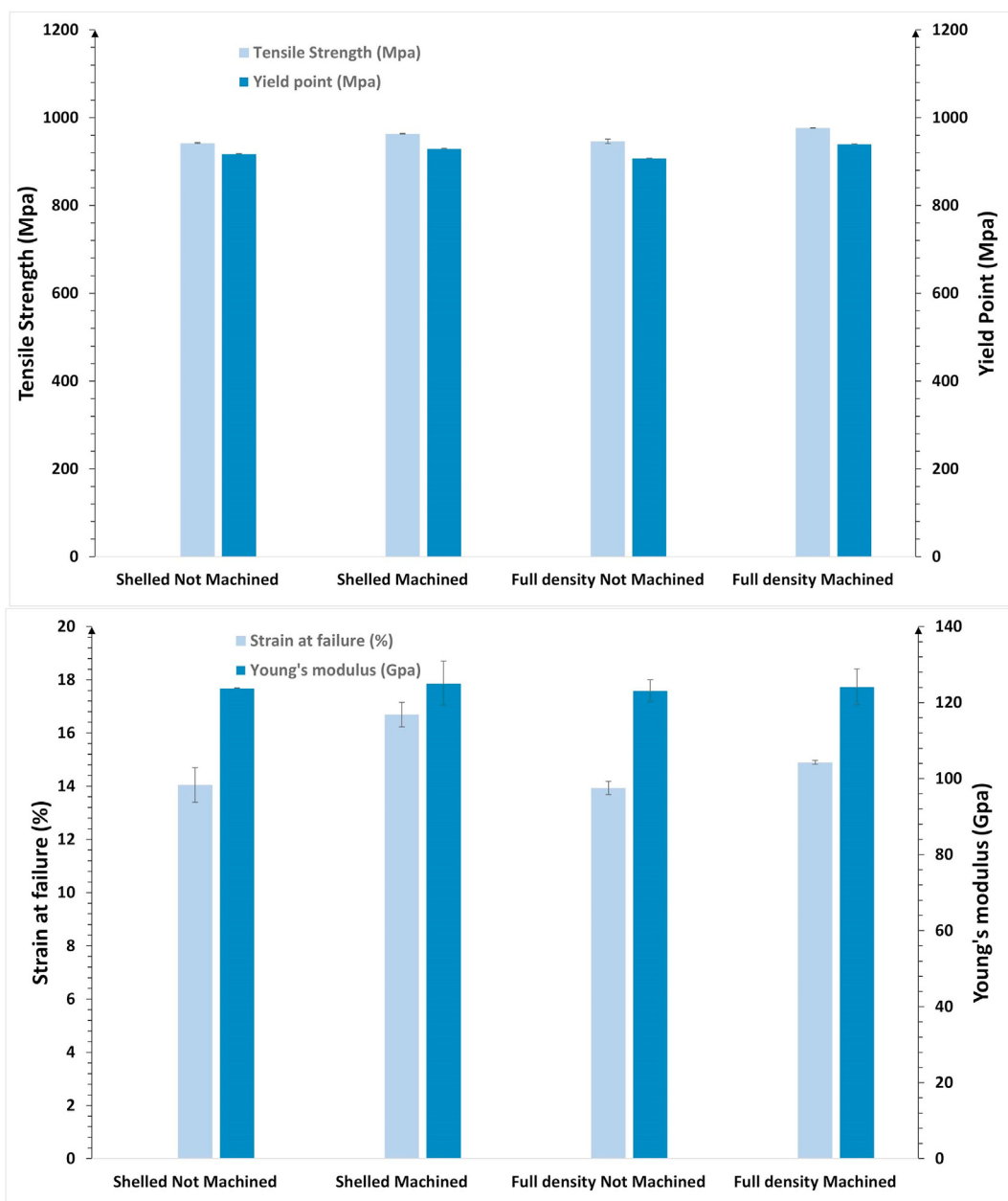


Fig. 10. Mechanical properties of the Machined and Not Machined parts based on the full density and shell conformation, all samples subjected to HIP.

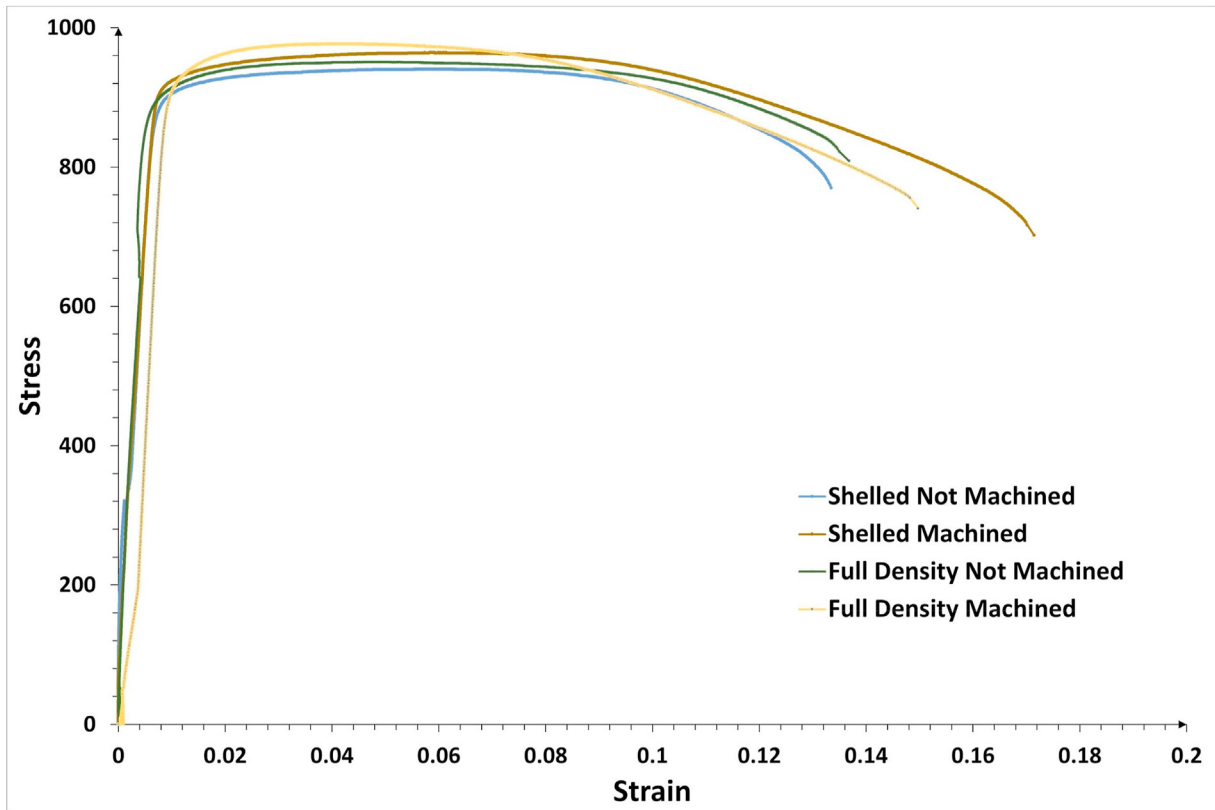


Fig. 11. Stress-Strain Curves of the Machined and Not Machined parts based on the full density and shell conformation, all samples subjected to HIP.

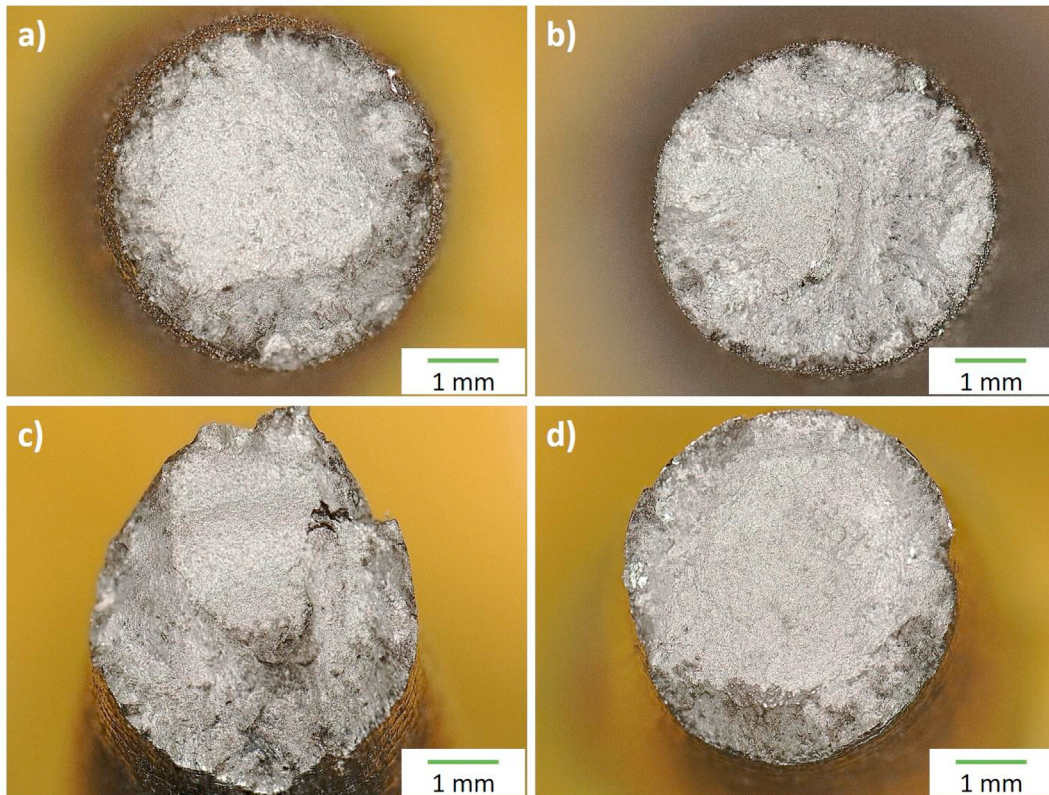


Fig. 12. Optical images of fractured tensile specimens, all HIPed: a) Shelled dogbone geometry. b) Solid dogbone c) Shelled machined and d) Solid machined.

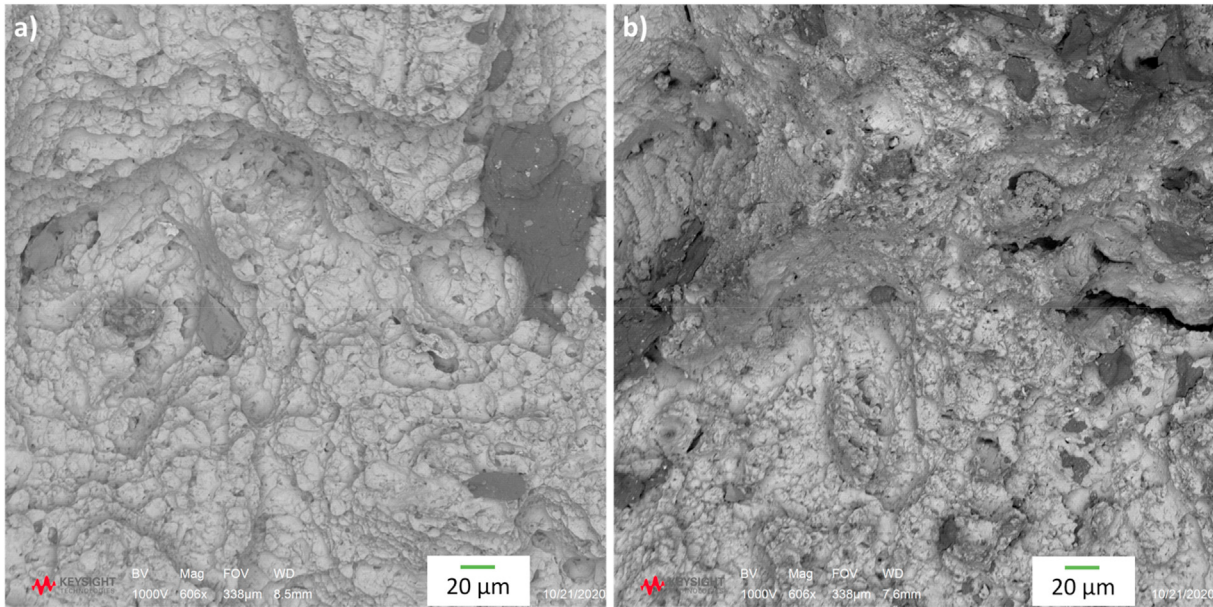


Fig. 13. SEM images of fractured tensile specimens. a) Solid machined and b) Shelled machined.

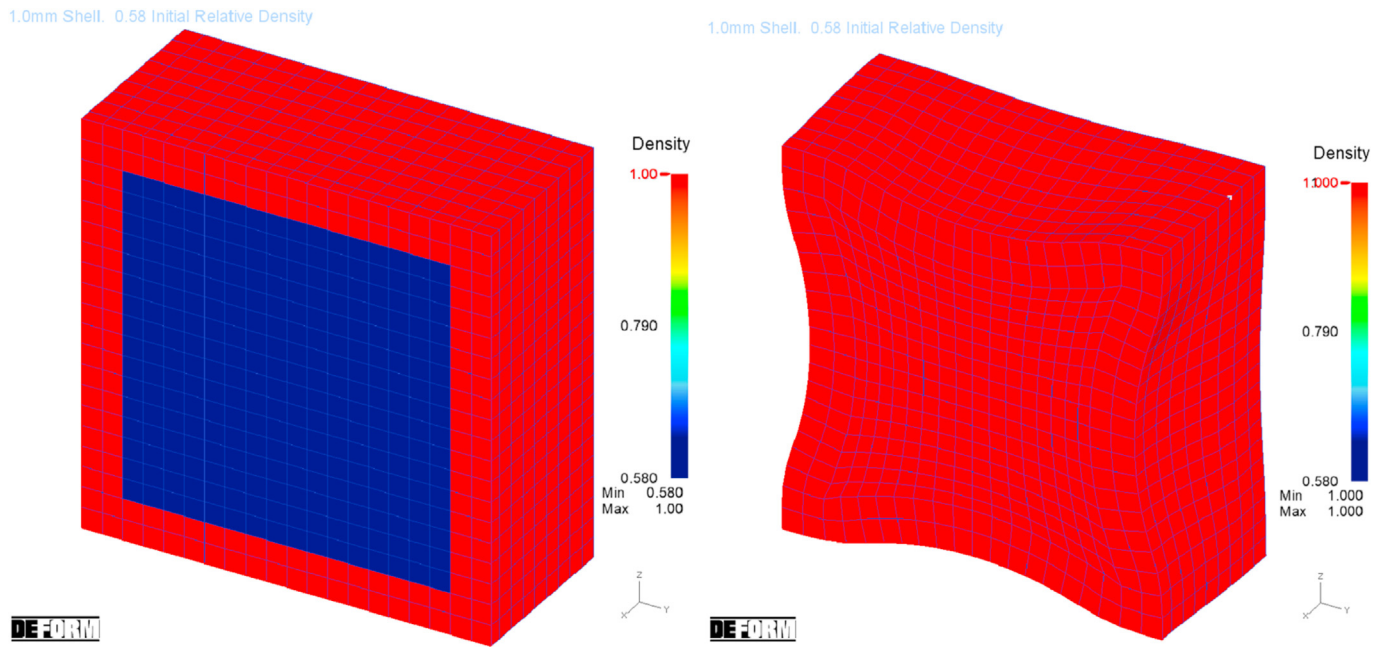


Fig. 14. Deformation simulation of 10 mm cube with 1 mm shell: elemental relative densities in the initial and HIP processed coupon.

3.3. HIP process simulation compared to real geometries

DEFORM-3D simulation results of the cubic coupons evaluated the impact of hybrid L-PBF design parameters on the HIP process output. The distortion of a 1 mm shell cube is shown in Fig. 14. The distortion pattern shown here was typical for all shell thicknesses. The distortion was most severe with thin shell sections and became less severe as shell thickness increased, as also confirmed by CT scans post-HIP shown in Fig. 8.

DEFORM-3D simulations performed on the bracket geometry revealed distortion behavior on an industrially-representative component. The simulated shelled bracket geometry is shown in Fig. 15 and the actual CT scans of the shelled bracket before and after HIP are shown in

Fig. 16. Significant warping was noted, along the thin structure connecting the bottom bosses, which drives substantial misalignment of the side bosses. This suggests an opportunity for future research studying the impact of structural geometries on distortion, leveraging high fidelity deformation simulations. This result also further validates the process in that the shelled geometry can be successfully densified.

3.4. Distortion compensation

Given the distortions involved in the HIP process (shown above), the development of a distortion compensated print geometry is required if the target geometry is to be achieved after the HIP process. A

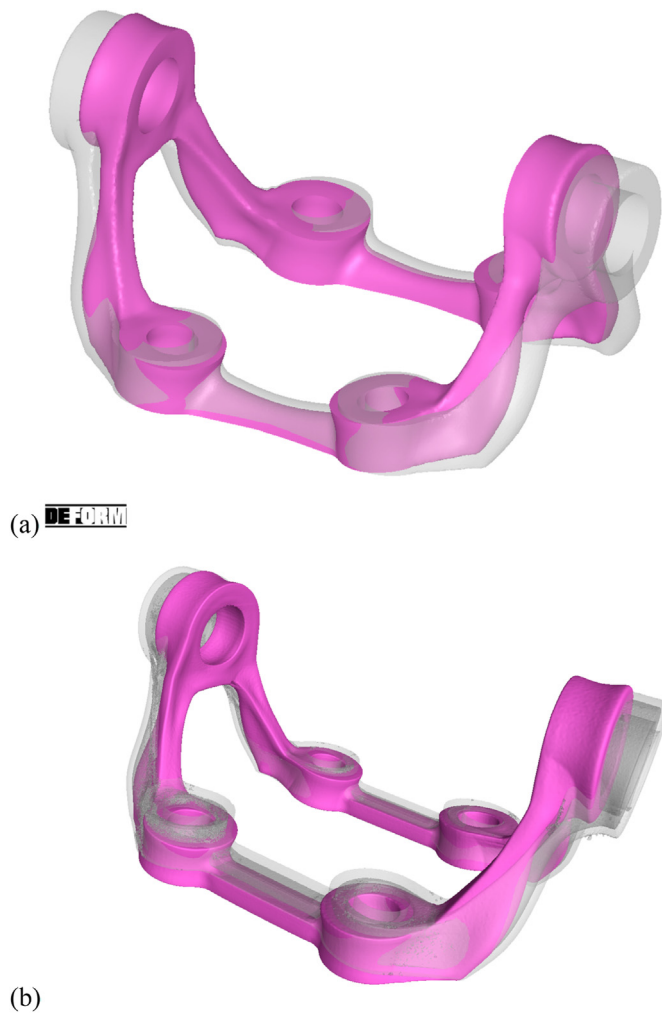


Fig. 15. Bracket results for shelled sample before (transparent) and after HIP (purple): (a) simulation results and (b) CT scans.

methodology was developed to compensate the target geometry using HIP process simulation of the uncompensated geometry.

The first-order compensation method utilized the distortion from the uncompensated model (Fig. 17), which was then inversely applied to the target shape. The result is a compensated, L-PBF produced shape as shown in both simulation and CT scan, Fig. 18. Higher-order optimization methodologies could be applied in future studies for more refined

compensation. Simulation results (Fig. 18) revealed that the shape of the compensated model matched the target geometry well following the HIP process.

The deformation compensation for HIP processing demonstrated above has some potential additional advantages, compared to building solid parts by L-PBF and subsequent HIPing. Besides the time saving of this process, bulky solid parts in L-PBF are prone to residual stress buildup which can lead to cracks or deformation (if connected to the surface of the part, this makes HIP ineffective and the crack cannot be healed). Building only shelled parts leads to less heat input and hence less residual stress, but this additional benefit requires further investigation.

3.5. Build times

In theory, a full build of a solid cube of $240 \times 240 \times 290$ mm is estimated to take 836 h, while the equivalent shelled version with 1.5 mm shell thickness is 61 h, a theoretical order of magnitude time saving (factor of 13.7 improvement) as summarized in Table 2. The example is an upper limit and not practical, hence a direct record of the build times in this work was done as a realistic time saving estimate. In the builds in this work, the shelled version included many cubes with thicker shells than needed, and many support structures were included for the bracket, reducing the time saving. The less-than-ideal build configuration highlights the importance of build planning for time saving in the context of HIP productivity improvement as well as optimizing not only the geometry for ensuring build success, but also limiting supports and unnecessary thick shells or fillets. Despite the relatively small and low number of parts in this study, and despite the use of significant supports and thicker shells than needed, a time saving of 12% was realized.

The build time saving of up to an order of magnitude for large builds can potentially reduce manufacturing costs by an order of magnitude as the manufacturing cost is directly related to the build time. This is assuming the HIP process is required with or without shell geometries, hence not adding cost to the new hybrid process, the time and cost saving of the L-PBF process is significant.

4. Conclusions

We lay the foundation for a new hybrid process of laser powder bed fusion of shelled parts followed by HIP, which allows up to an order of magnitude faster production time on typical L-PBF systems. This has significant benefits for cost reduction while potentially reducing residual stress related problems in bulky parts. This work reports numerous interesting results which can be used to further develop the process. One concern is the presence of Argon gas in the part - the HIP process is shown here to close all pores below the resolution of the microCT scan, but some small porosity may still be present - as the pores are compressed to small size. In this work, good mechanical properties were found, but in

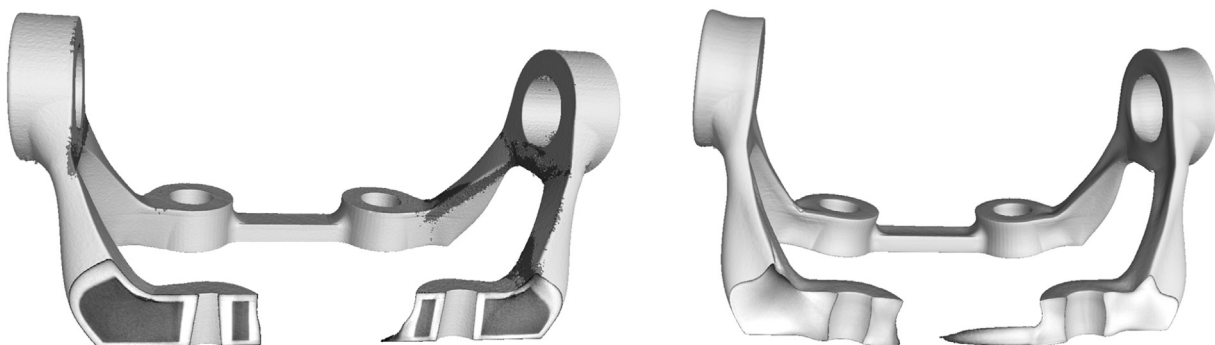


Fig. 16. CT scans of shelled bracket before (left) and after HIP (right), showing densification and deformation.

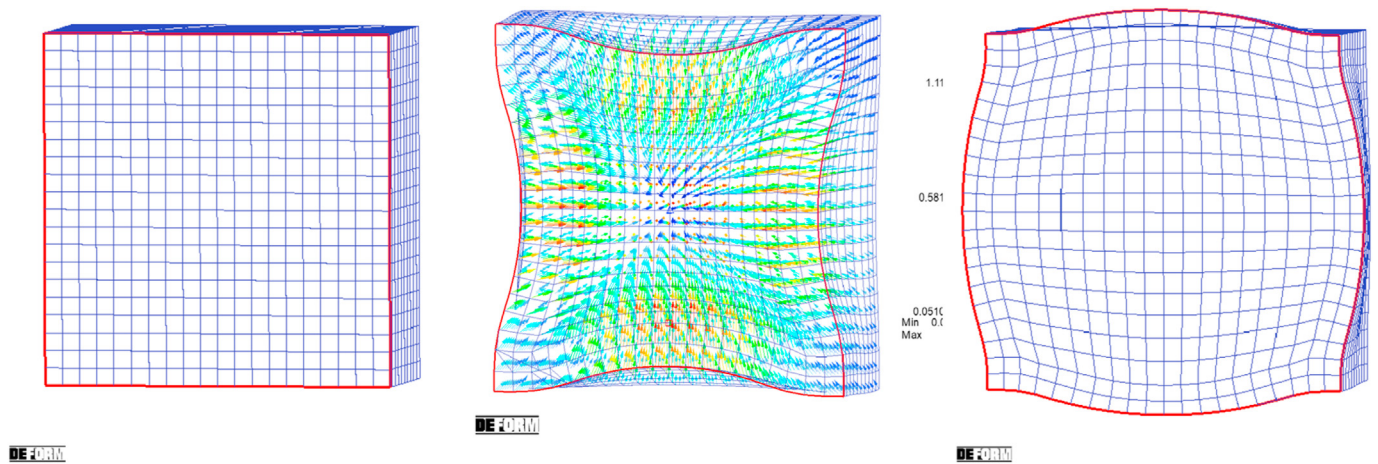


Fig. 17. Original (left) and compensated (right) models for the 1.0 mm shelled cube coupon. Nodal displacement vectors were extracted from the original simulation (center) and applied to the original cube model to derive the compensated model.

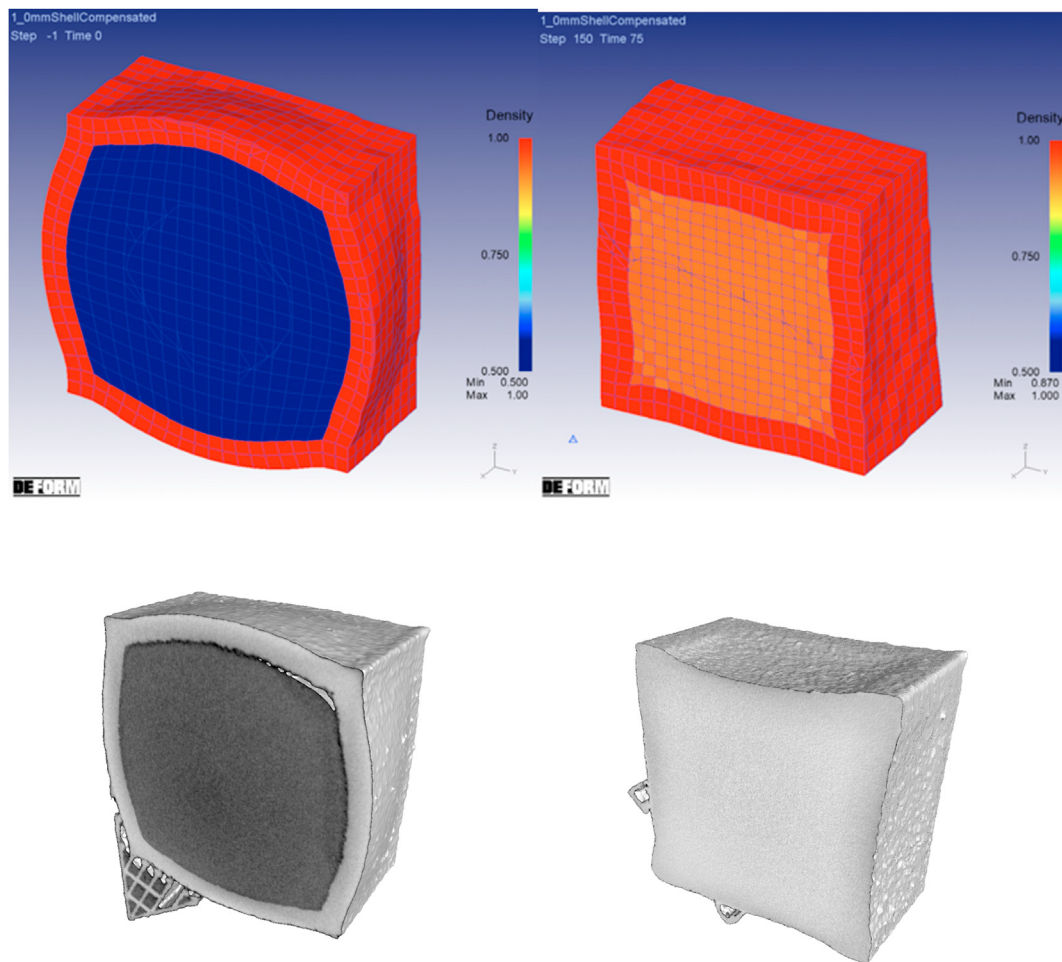


Fig. 18. Simulations of HIP processing of compensated cube (top) and microCT scans of compensated cube (bottom) before and after HIP (support structures still attached, seen to the left).

complex and larger geometries, larger pore spaces may result which may be more difficult to close sufficiently by HIP. More experimentation is needed to resolve if this will affect mechanical properties. Further work is also required to test the limits of the method, refine new design and part

placement rules to allow good build quality for shelled parts (e.g. using internal fillets as shown) and validate deformation compensation for larger and more complex parts. Overall, this process shows great promise for enhancing the production rates in L-PBF additive manufacturing.

Table 2
Overview of all manufactured samples.

	Solid	Shelled
Cube 240 × 240 × 290 mm (maximum possible size EOS M290)	836h05	61h22
Builds in this work	9h53	8h48

Declaration of competing interest

The authors declare the following financial interests/personal relationships which may be considered as potential competing interests: One author works for a company selling HIP equipment, and some authors work for a software company performing deformation simulation. These are not considered conflicts in this work.

Acknowledgements

We would like to highlight the support from the Murchison Chair at the University of Texas at El Paso. AdP is also thankful for financial support from the South African Collaborative Program in Additive Manufacturing (CPAM).

Appendix A. Supplementary data

Supplementary data to this article can be found online at <https://doi.org/10.1016/j.aime.2021.100031>.

References

- Ahlfors, M., Bahbou, F., Eklund, A., Ackelid, U., 2019. HIP for AM-optimized material properties by HIP. *Mater Res Proc* 1–10. mrforum.com.
- Atkinson, H.V., Davies, S., 2000. Fundamental aspects of hot isostatic pressing: an overview. *Metall. Mater. Trans.* 31, 2981–3000.
- Cai, C., Song, B., Xue, P., Wei, Q., Yan, C., Shi, Y., 2016a. A novel near α -Ti alloy prepared by hot isostatic pressing: microstructure evolution mechanism and high temperature tensile properties. *Mater. Des.* 106, 371–379.
- Cai, C., Song, B., Xue, P., Wei, Q., Wu, J.-M., Li, W., et al., 2016b. Effect of hot isostatic pressing procedure on performance of Ti6Al4V: surface qualities, microstructure and mechanical properties. *J. Alloys Compd.* 686, 55–63.
- Cai, C., Gao, X., Teng, Q., Li, M., Pan, K., Song, B., et al., 2018. A novel hybrid selective laser melting/hot isostatic pressing of near-net shaped Ti-6Al-4V alloy using an in-situ tooling: interfacial microstructure evolution and enhanced mechanical properties. *Mater. Sci. Eng., A* 717, 95–104.
- Carter, W., Tucker, M., Mahony, M., Toledano, D., Butler, R., Roychowdhury, S., et al., 2020a. An open-architecture multi-laser research platform for acceleration of large-scale Additive manufacturing (ALSAM). Available: <https://works.bepress.com/Sara-Bose/52/download/>.
- Carter, W.T., Graham, M.E., Hayden, C.J., Jeong, Y., Mamrak, J., McCarthy, B.S., et al., 2020b. A large format DMLM system using a continuously rotating powder bed. *Additive Manufact.* 31, 100983.
- Chastand, V., Quaegebeur, P., Maia, W., Charkaluk, E., 2018. Comparative study of fatigue properties of Ti-6Al-4V specimens built by electron beam melting (EBM) and selective laser melting (SLM). *Mater. Char.* 143, 76–81.
- Das, S., Wohler, M., Beaman, J.J., Bourell, D.L., 1999. Processing of titanium net shapes by SLS/HIP. *Mater. Des.* 20, 115–121.
- de Formanoir, C., Paggi, U., Colebrants, T., Thijs, L., Li, G., Vanmeensel, K., et al., 2020. Increasing the productivity of laser powder bed fusion: influence of the hull-bulk strategy on part quality, microstructure and mechanical performance of Ti-6Al-4V. *Additive Manufact.* 33, 101129.
- DebRoy, T., Wei, H.L., Zuback, J.S., Mukherjee, T., Elmer, J.W., Jo, Milewski, et al., 2017. Additive manufacturing of metallic components—process, structure and properties. *Prog. Mater. Sci.* Available: <https://www.sciencedirect.com/science/article/pii/S0079642517301172>.
- du Plessis, A., le Roux, S.G., 2018. Standardized X-ray tomography testing of additively manufactured parts: a round robin test. *Additive Manufact.* 24, 125–136.
- du Plessis, A., Macdonald, E., 2020. Hot isostatic pressing in metal additive manufacturing: X-ray tomography reveals details of pore closure. *Additive Manufact.* 101191.
- du Plessis, A., Rossouw, P., 2015. Investigation of porosity changes in cast Ti6Al4V rods after hot isostatic pressing. *J. Mater. Eng. Perform.* 24, 3137–3141.
- du Plessis, A., le Roux, S.G., Guelpa, A., 2016. The CT Scanner Facility at Stellenbosch University: an open access X-ray computed tomography laboratory. *Nucl. Instrum. Methods Phys. Res. B* 384, 42–49.
- Du Plessis, A., Yadroitsava, I., Yadroitssev, I., le Roux, S.G., Blaine, D.C., 2018a. Numerical comparison of lattice unit cell designs for medical implants by additive manufacturing. *Virtual Phys. Prototyp.* 13, 266–281.
- Du Plessis, A., Yadroitssev, I., Yadroitsava, I., Le Roux, S.G., 2018b. X-ray microcomputed tomography in additive manufacturing: a review of the current technology and applications. *3D Print. Addit. Manuf.* 5, 227–247.
- du Plessis, A., le Roux, S.G., Waller, J., Sperling, P., Achilles, N., Beerlink, A., et al., 2019. Laboratory X-ray tomography for metal additive manufacturing: round robin test. *Additive Manufact.* 30, 100837.
- Eklund, A., Ahlfors, M., Bahbou, F., Wedenstrand, J., 2018. Optimizing HIP and printing parameters for EBM Ti-6Al-4V. In: *Key Engineering Materials*. Trans Tech Publ, pp. 174–178.
- Flores, I., Kretschmar, N., Azman, A.H., Chekurov, S., Pedersen, D.B., Chaudhuri, A., 2020. Implications of lattice structures on economics and productivity of metal powder bed fusion. *Additive Manufact.* 31, 100947.
- Galaraga, H., Warren, R.J., Lados, D.A., Dehoff, R.R., Kirka, M.M., Nandwana, P., 2017. Effects of heat treatments on microstructure and properties of Ti-6Al-4V ELI alloy fabricated by electron beam melting (EBM). *Mater. Sci. Eng., A* 685, 417–428.
- Goel, S., Ahlfors, M., Bahbou, F., Joshi, S., 2019. Effect of different post-treatments on the microstructure of EBM-built alloy 718. *J. Mater. Eng. Perform.* 28, 673–680.
- Gu, D.D., Meiners, W., Wissenbach, K., Poprawe, R., 2012. Laser additive manufacturing of metallic components: materials, processes and mechanisms. *Int. Mater. Rev.* 57, 133–164.
- Herzog, D., Bartsch, K., Bossen, B., 2020. Productivity optimization of laser powder bed fusion by hot isostatic pressing. *Additive Manufact.* 36, 101494.
- Hosseini, A.M., Masood, S.H., Fraser, D., Jahedi, M., 2012. Mechanical properties investigation of HIP and as-built EBM parts. In: *Advanced Materials Research*. Trans Tech Publ, pp. 216–219.
- Kaplanski, Y.Y., Zaitsev, A.A., Levashov, E.A., Loginov, P.A., Sentyurina, Z.A., 2018. NiAl based alloy produced by HIP and SLM of pre-alloyed spherical powders. Evolution of the structure and mechanical behavior at high temperatures. *Mater. Sci. Eng., A* 717, 48–59.
- Kunz, J., Kaletsch, A., Broeckmann, C., 2016. Influence of HIP post-treatment on the fatigue strength of 316L-steel produced by selective laser melting (SLM). In: *European Congress and Exhibition on Powder Metallurgy European PM Conference Proceedings*. The European Powder Metallurgy Association, pp. 1–6.
- Kunz, J., Saewe, J., Herzog, S., Kaletsch, A., Schleifenbaum, J.H., Broeckmann, C., 2020. Mechanical properties of high-speed steel AISI M50 produced by laser powder bed fusion. *Steel Res. Int.* 91, 1900562.
- Leicht, A., Sundaram, M.V., Yao, Y., Hryha, E., Nyborg, L., Rännar, L.-E., et al., 2016. As-HIP microstructure of EBM fabricated shell components. In: *European Congress and Exhibition on Powder Metallurgy European PM Conference Proceedings*. The European Powder Metallurgy Association, pp. 1–6.
- Leuders, S., Thöne, M., Riemer, A., Niendorf, T., Tröster, T., Richard, H.A., et al., 2013. On the mechanical behaviour of titanium alloy TiAl6V4 manufactured by selective laser melting: fatigue resistance and crack growth performance. *Int. J. Fatig.* 48, 300–307.
- Liu, S., Shin, Y.C., 2019. Additive manufacturing of Ti6Al4V alloy: a review. *Mater. Des.* 164, 107552.
- Ma, M., Wang, Z., Gao, M., Zeng, X., 2015. Layer thickness dependence of performance in high-power selective laser melting of 1Cr18Ni9Ti stainless steel. *J. Mater. Process. Technol.* 215, 142–150.
- Magnus Ahlfors Chad Beamer, 2020. Print faster with lower energy input in powder bed fusion Ti-6Al-4V using hot isostatic pressing (HIP) quintus technologies. Rapid 2020 (cancelled due to the pandemic).
- Masuo, H., Tanaka, Y., Morokoshi, S., Yagura, H., Uchida, T., Yamamoto, Y., et al., 2018. Influence of defects, surface roughness and HIP on the fatigue strength of Ti-6Al-4V manufactured by additive manufacturing. *Int. J. Fatig.* 117, 163–179.
- Medina, F., 2013. Reducing Metal Alloy Powder Costs for Use in Powder Bed Fusion Additive Manufacturing: Improving the Economics for Production. University of Texas at El Paso. Available: https://scholarworks.utep.edu/open_etd/1678/.
- Mireles, J., Ridwan, S., Morton, P.A., Hinojos, A., Wicker, R.B., 2015. Analysis and correction of defects within parts fabricated using powder bed fusion technology. *Surf. Topogr. Metrol. Prop.* 3, 034002.
- Montero-Sistiaga, M.L., Pourbabak, S., Van Humbeeck, J., Schryvers, D., Vanmeensel, K., 2019. Microstructure and mechanical properties of Hastelloy X produced by HP-SLM (high power selective laser melting). *Mater. Des.* 165, 107598.
- Mostafa, A., Picazo Rubio, I., Brailovski, V., Jahazi, M., Medraj, M., 2017. Structure, texture and phases in 3D printed IN718 alloy subjected to homogenization and HIP treatments. *Metals* 7, 196. Oh et al., 1987. Oh, S.I., Wu, W.T., Park, J.J., 1987. Application of the finite element method to P/M forming processes. In: *Proceedings of the 2nd International Conference on the Technology of Plasticity*, Stuttgart, Germany.
- Persnot, T., Martin, G., Dendievel, R., Buffière, J.-Y., Maire, E., 2018. Enhancing the tensile properties of EBM as-built thin parts: effect of HIP and chemical etching. *Mater. Char.* 143, 82–93.
- Plocher, J., Panesar, A., 2020. Effect of density and unit cell size grading on the stiffness and energy absorption of short fibre-reinforced functionally graded lattice structures. *Additive Manufact.* 33, 101171.
- Poprawe, R., Hinke, C., Meiners, W., Schrage, J., 2015. SLM production systems: recent developments in process development, machine concepts and component design. *Adv. Prod.* Available: <https://www.oapen.org/download?type=document&docid=1001851#page=58>.
- Riehm, S., Kaletsch, A., Broeckmann, C., Friederici, V., Wieland, S., Petzoldt, F., 2019. Tailor-made net-shape composite components by combining additive manufacturing and hot isostatic pressing. *Hot Isostatic Pressing: HIP'17* 10, 203.
- Schneller, W., Leitner, M., Springer, S., Grün, F., Taschauer, M., 2019. Effect of HIP treatment on microstructure and fatigue strength of selectively laser melted AlSi10Mg. *J. Mater. Process. Manuf. Sci.* 3, 16.

- Seifi, M., Salem, A.A., Satko, D.P., Ackelid, U., Semiatin, S.L., Lewandowski, J.J., 2017a. Effects of HIP on microstructural heterogeneity, defect distribution and mechanical properties of additively manufactured EBM Ti-48Al-2Cr-2Nb. *J. Alloys Compd.* 729, 1118–1135.
- Seifi, M., Gorelik, M., Waller, J., Hrabec, N., Shamsaei, N., Daniewicz, S., et al., 2017b. Progress towards metal additive manufacturing standardization to support qualification and certification. *JOM* 69, 439–455.
- Standard A. ISO/ASTM 52900: 2015, 2012. Additive Manufacturing-General Principles-Terminology. ASTM F2792-10e1.
- Uzan, N.E., Ramati, S., Shneck, R., Frage, N., Yeheskel, O., 2018. On the effect of shot-peening on fatigue resistance of AlSi10Mg specimens fabricated by additive manufacturing using selective laser melting (AM-SLM). *Additive Manuf.* 21, 458–464.
- Van Grunsven, W., Hernandez-Nava, E., Reilly, G.C., Goodall, R., 2014. Fabrication and mechanical characterisation of titanium lattices with graded porosity. *Metals* 4, 401–409.
- DEFORM Version 12.0.1, 2020. Scientific Forming Technologies Corporation, Columbus Ohio.
- Wu, W.T., Tang, J.P., Li, G., 2000. Recent developments of process simulation and its application to manufacturing processes. In: Proceedings of the 1st International Conference on Thermal Process Modeling and Computer Simulation, Shanghai, P.R. China.
- Yan, X., Lupoi, R., Wu, H., Ma, W., Liu, M., O'Donnell, G., et al., 2019. Effect of hot isostatic pressing (HIP) treatment on the compressive properties of Ti6Al4V lattice structure fabricated by selective laser melting. *Mater. Lett.* 255, 126537.
- Zhou, J., Zhang, Y., Chen, J.K., 2009. Numerical simulation of random packing of spherical particles for powder-based additive manufacturing. *J. Manuf. Sci. Eng.* 131 <https://doi.org/10.1115/1.3123324>.
- Zhou, B., Zhou, J., Li, H., Lin, F., 2018. A study of the microstructures and mechanical properties of Ti6Al4V fabricated by SLM under vacuum. *Mater. Sci. Eng., A* 724, 1–10.